



Nanoindentation and nanoscratching of iron: Atomistic simulation of dislocation generation and reactions



Yu Gao^a, Carlos J. Ruestes^b, Herbert M. Urbassek^{a,*}

^a Physics Department and Research Center OPTIMAS, University Kaiserslautern, Erwin-Schrödinger-Straße, D-67663 Kaiserslautern, Germany

^b Instituto de Ciencias Básicas, Universidad Nacional de Cuyo, Mendoza 5500, Argentina

ARTICLE INFO

Article history:

Received 5 January 2014

Received in revised form 3 April 2014

Accepted 5 April 2014

Available online 8 May 2014

Keywords:

Molecular dynamics

Nanoindentation

Nanoscratching

Iron

Dislocations

Plasticity

Twinning

ABSTRACT

Using molecular-dynamics simulation, we study nanoindentation and scratching in an Fe (100) surface. We find an indentation hardness of 20 GPa in good agreement with experiment and previous simulations. The length of the dislocations generated and the volume of the plastic zone follow a simple model based on the dislocations necessary to remove the material from the indentation zone, the so-called geometrically necessary dislocations. The dislocation density stays approximately constant. Both $\mathbf{b} = \frac{1}{2}\langle 111 \rangle$ and $\mathbf{b} = \langle 100 \rangle$ dislocations contribute to the plastic zone. During scratching, we observe a distinct re-organization of the dislocation network; the reaction of $\mathbf{b} = \frac{1}{2}\langle 111 \rangle$ to $\mathbf{b} = \langle 100 \rangle$ dislocations plays an important role. After longer scratching the dislocations in the middle of the scratch groove react and the dislocation density there is strongly reduced; all further dislocation activity occurs at the scratch front. Deformation twinning is observed both in the indentation and in the scratch stage. Both normal and lateral scratch hardness decrease with depth, while the friction coefficient shows a strong increase.

© 2014 Elsevier B.V. All rights reserved.

1. Introduction

Nanoindentation constitutes a standard technique for the analysis of the mechanical properties of materials [1,2]. It immediately provides information on the elastic properties of the substrate and on its hardness. Nowadays computer simulation based on the molecular-dynamics method is able to provide detailed information on the processes occurring under nanoindentation; when applied to single crystals, it gives results in good agreement with experiment [3,4]. In addition, due to the versatility of computer simulation, the influence of materials properties on the indentation can readily be investigated [5,6]. The process of scratching – sometimes denoted as ‘ploughing’ [7] – where an indented tip is moved parallel to the surface, constitutes a comparatively simple scenario, in which the lateral mechanic response of a substrate is tested; such experiments provide information on the friction coefficient and thus on a tribological quantity of prime importance [8].

When applied to elemental materials, both nanoindentation [9–18] and nanoscratching [7,19–24] simulations have mostly been performed for fcc metals such as Cu, Al or Au. Simulations of indentation in bcc metals are more rare – despite a considerable body of

experimental data [25] – and include work on W [26], Ta [27,28] and Fe [4,29–32]; for nanoscratching only Fe substrates appear to have been simulated [7,33].

Previous simulation results describe the atomistic processes occurring in bcc metals during plastic deformation initiated by the indentation process. Smith et al. [30] describe the defect generation and pile-up of atoms during nanoindentation of Fe single crystals. Hagelaar et al. [26] characterize the formation and destruction of nanoindentation contacts of a W tip in W. Biener et al. [27] investigate defect nucleation under nanoindentation in Ta; this work is continued by Alcalá et al. [28] who focus on dislocation and planar-defect formation. Lu et al. [4] show that simulated nanoindentation results in Fe are in good agreement with experimental data. Mulliah et al. [7] discuss in detail friction coefficients obtained for nanoscratching an Fe surface and find a strong depth dependence.

Of particular interest in the field of nanoindentation is the so-called indentation size effect: the indentation hardness has been found to depend on the relevant length scale, which is primarily defined by the indentation depth. This effect is both found in experiment and simulation and has been reviewed by Durst et al. [34]. Our work contributes to the understanding of this effect in that we extend it also to nanoscratching.

In this paper we study indentation and scratching for a prototypical bcc material, α -Fe. We focus on the characterization of

* Corresponding author. Tel.: +49 631 205 3022; fax: +49 631 205 3907.

E-mail address: urbassek@hrk.uni-kl.de (H.M. Urbassek).

URL: <http://www.physik.uni-kl.de/urbassek/> (H.M. Urbassek).

the dislocations generated in these processes and on their evolution and reactions. In addition, we discuss the material hardness, the dependence of the friction coefficient on the scratch depth and the debris created on the surface. We provide novel data on the generation of dislocations, point defects and twins during indentation and scratching and show how dislocation reactions during scratch modify the dislocation network. The length of the dislocation network and the dislocation density are in agreement with a simple geometrical model.

2. Simulation method

We employ molecular-dynamics simulation to study the behavior of an Fe single crystal during nanoindentation and scratching. Fig. 1 shows a schematic representation of the molecular-dynamics (MD) simulation system. It illustrates the configuration of the nanoindenter and the Fe substrate. Our simulation consists of three parts: (i) nanoindentation, during which the indenter is pushed in the z direction into the substrate; (ii) nanoscratching: the indenter moves at the indentation depth along the x direction; and (iii) retraction of the indenter: the indenter is moved out of the substrate to return to the initial height.

The nanoindenter has a spherical shape with a radius of $R = 21.4$ Å. It consists of 7248 C atoms arranged in a diamond lattice structure. It is rigid during the simulation; i.e., all C atoms move as a rigid body. We note that in previous nanoscratch simulations indenters of various composition have been used. Refs. [22,24,33] employ an indenter which is given by a repulsive potential surface; this indenter is not atomically resolved. Refs. [23,35] use an atomistically resolved indenter, which is rigid and interacts with both attractive and repulsive forces to the substrate. Finally, Refs. [7,20,21] employ an atomistic indenter with free atoms, which however interacts via repulsive and in one case with both repulsive and attractive forces with the substrate; in Ref. [7] even the interaction of the indenter tip with the AFM apparatus is modeled via elastic spring forces. Free indenter atoms with attractive forces would allow to monitor tip-substrate chemistry (so-called tribo-chemistry); the sophisticated model of Ref. [7] was set up to study in detail the so-called stick-slip phenomenon

encountered in friction. In the present study we utilize the relatively modest rigid repulsive indenter model, since our present interest is not in tribo-chemistry nor in the complications arising due to stick-slip motion.

The substrate is a bcc iron single crystal with a (100) surface. The cartesian coordinate system is aligned with the (100) crystal directions, such that indentation is along $-z$ and scratching is along x , see Fig. 1. The Fe substrate in our simulation has dimensions of 314 Å, 314 Å, and 200 Å in the x , y , and z directions, respectively. It consists of 1,694,000 atoms. We checked that the box is large enough to avoid the generated dislocations to reach the boundaries of the simulation box. Two atom layers at the bottom are fixed in order to suppress any rigid-body movement of the substrate during nanoscratching [24]. The next four layers at the bottom, as well as the outermost four layers of the substrate in lateral directions are kept at a fixed temperature of 0 K by a Nosé-Hoover thermostat; this low temperature has been adopted to get rid of all thermally activated processes. In addition, periodic boundary conditions are applied in the lateral x and y directions. The top surface is free.

In order to assess the influence of target temperature we performed an indentation simulation at 300 K. The results are in qualitative agreement with the 0 K results presented here. Quantitatively, we see an increase of the total dislocation length by 5.5% and a decrease of the indentation hardness of 12%. Mulliah et al. [7] simulated the scratch process in Ag at 0 K and at 300 K and conclude that ‘the value of both the dynamic and the static friction coefficients of Ag agree almost exactly’.

The Fe-Fe interaction is described by the Mendelev potential [36], which is smoothly cut-off at 5.4 Å. In our simulation the interaction between the diamond indenter and the iron substrate is modeled by a purely repulsive potential; this is obtained from a Lennard-Jones potential [37], which is cut-off at 4.2 Å at its minimum and then shifted such as to have continuous energy and force at the cut-off radius.

Before performing the nanoindentation and the nanoscratching simulations, the iron substrate is relaxed at a temperature of 0 K until all stress components have reached values $< 10^{-5}$ GPa [17]. The center of the indenter is placed at a height of 26 Å above the substrate surface such that all indenter atoms are outside the cut-off range of the Fe-C interaction potential. After that the nanoindentation and nanoscratching simulations are performed. The indenter moves with a constant velocity of $v = 10$ m/s, both in the indentation and in the scratching process. The simulation is performed in the so-called velocity-controlled way; that is, at every MD time step Δt , the indenter proceeds rigidly by a path length $v \cdot \Delta t$. The indenter penetrates the substrate until a depth d ; we penetrate up to a maximum depth of 21.4 Å, equal to the indenter radius. The scratch length L is 50 Å. Thus the indentation time amounts to 260 ps, and the scratching time to 500 ps. The retraction process is simulated analogous to the indentation.

The MD simulations are performed using the open-source LAMMPS code [38] with a constant time step of 1 fs. In order to identify the lattice dislocations and to determine their Burgers vectors, the dislocation extraction algorithm (DXA) is used [39]. It is based on the common-neighbor analysis method [40] to identify the local crystallographic structure in the neighborhood of each atom. Dislocation cores are identified by performing Burgers circuits and shrinking them as far as possible. The positions of the dislocation cores are used to construct the one-dimensional dislocation lines. This allows both to calculate the number of dislocations and to measure the length of dislocation lines. In addition, the Crystal Analysis Tool (CAT) is employed to identify particular defects, such as twins [41–43]. For visualization of the atomistic configurations we use the free software tools Atomeye [44], ParaView [45] and OVITO [46].

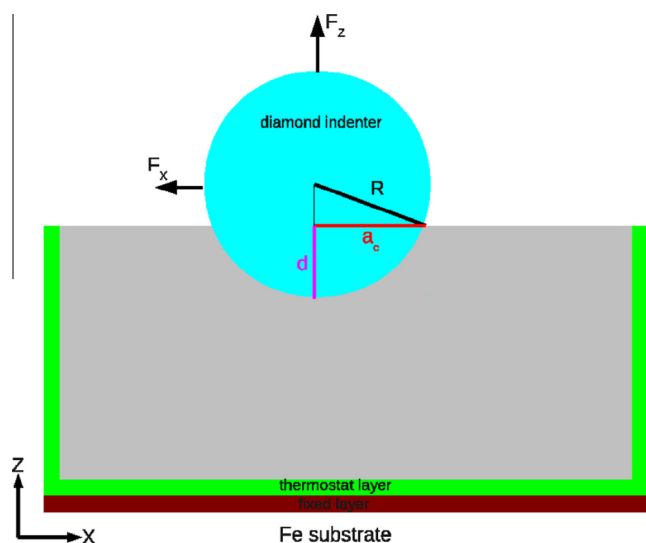


Fig. 1. Setup of the simulation system. The radius R of the indenter, its indentation depth d , and the contact-area radius a_c are indicated. Indentation force F_z as well as scratching force F_x are shown. The substrate has thermostatting and rigid zones at its boundaries.

3. Results

3.1. Indentation

Fig. 2(a) shows the normal force exerted on the indenter, F_z , as a function of indentation depth d . The force is determined as the sum of the forces exerted by all Fe atoms on the indenter in the z direction, perpendicular to the surface. The force is purely repulsive since also the Fe–C interaction in our model is purely repulsive. The force starts increasing as soon as the indenter reaches the cut-off radius of the interaction potential, at -4.2 Å. Fig. 3 shows snapshots of the processes occurring under the indenter in the material, which are useful for understanding the force–displacement curve.

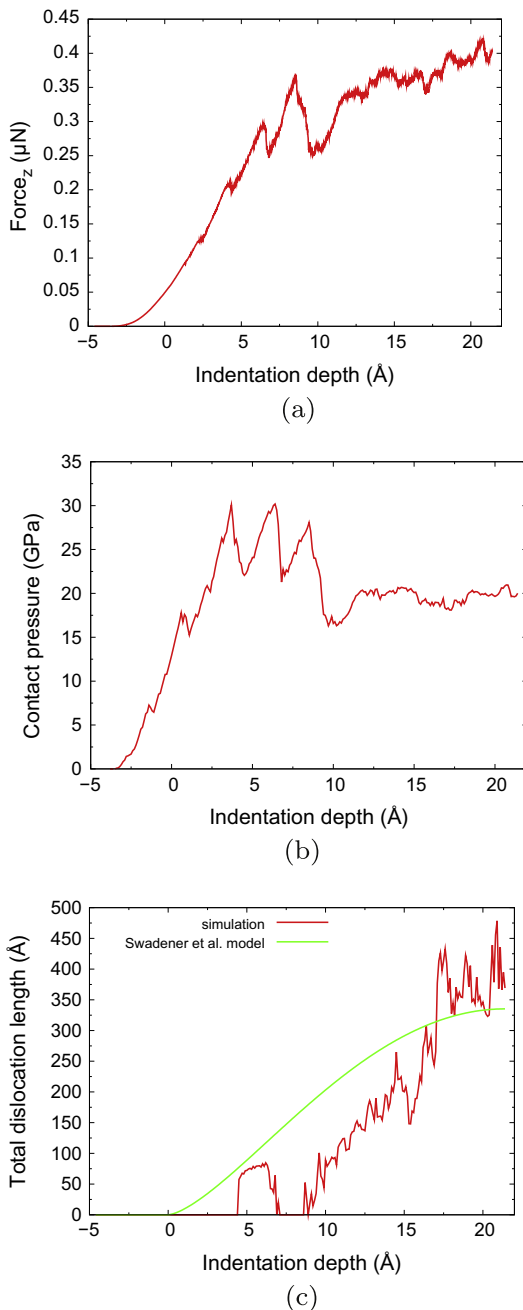


Fig. 2. (a) Normal force, (b) contact pressure, and (c) total dislocation length – including the model of Eq. (1) – vs. indentation depth during the indentation process.

Initially $F_z(d)$ follows the elastic Hertzian behavior. At this stage, no defects are seen in the material, as evidenced by Fig. 3 ($d = 2.4$ Å). The small fluctuation seen in Fig. 2(a) at $d = 3$ Å is due to the formation of a temporary defect, which does not lead to permanent dislocation generation. A more pronounced fluctuation of F_z is seen at $d = 4.5$ Å, where the force reaches 0.2 μN. Here, Fig. 3 shows that dislocations have been nucleated; two perfect dislocations with Burgers vector $\mathbf{b} = \frac{1}{2}\langle 111 \rangle$ are generated under the indented surface. When the indenter reaches depths of 6.8 and 9.7 Å, the third and the fourth dislocation with Burgers vector $\mathbf{b} = \frac{1}{2}\langle 111 \rangle$ successively appear. The force peaks in Fig. 2(a) correspond exactly to the occurrence of these dislocation nucleation events. Data on the evolution and generation of dislocations under indentation are collected in Table 1(a).

When the indenter reaches a depth of 15.4 Å, the number of dislocations has increased to six; only part of these are visible in the snapshots due to the viewing angle. Only two of these have Burgers vector $\mathbf{b} = \frac{1}{2}\langle 111 \rangle$, while four have $\mathbf{b} = \langle 100 \rangle$. Note that in bcc metals, in general, not only dislocations with the shortest Burgers vector, $\mathbf{b} = \frac{1}{2}\langle 111 \rangle$, exist; also dislocations with Burgers vector $\mathbf{b} = \langle 100 \rangle$ are formed during deformation by the interaction between dislocations with Burgers vector $\mathbf{b} = \frac{1}{2}\langle 111 \rangle$ [47,48]. Finally, when the indenter reaches its maximum depth of 21.4 Å, a total of 14 dislocations have been generated under the indented surface.

We determine the slip planes in which the dislocations evolve for a few exemplary cases. This is done as follows. The normal of the slip plane is obtained as the vector product of the dislocation line and its Burgers vector; in case these coincide – this happens for a screw segment – the slip plane normal is inferred from the neighboring dislocation segments. It is well known that in bcc metals slip is dominated by the $\{110\}\langle 111 \rangle$, $\{112\}\langle 111 \rangle$ and $\{123\}\langle 111 \rangle$ systems [47]. We found that all these slip systems are active during indentation and scratch; in addition we also find $\{100\}\langle 100 \rangle$ slip. This finding is in agreement with the recent study of Kumar et al. on nanoindentation of Fe [32].

Fig. 2(c) displays the total length, L_{disl} , of the dislocation lines formed during indentation. It quantifies the information of the snapshots, Fig. 3, described above. Note that the initially formed dislocations (depth of 4 Å) appear to decay again at around 7 Å. We presume that this is an artifact caused by the DXA detector: if dislocations are too close to the deformed substrate surface, they are not easily identified by a Burgers circuit, and may be misinterpreted as an ‘unidentified defect’ or as belonging to the surface.

Nix and coworkers were the first to calculate dislocation densities caused by a conical indenter [49,50]. These results were later generalized to a spherical indenter by Swadener et al. [51] using a paraboloid approximation. They predict a dislocation length of

$$L_{\text{disl}} = \frac{2\pi}{3} \frac{a_c^3}{bR}, \quad (1)$$

where

$$a_c = \sqrt{R^2 - (R - d)^2} \quad (2)$$

is the contact radius, and $b = 2.87$ Å is the length of the Burgers vector. Fig. 2(c) shows that this prediction describes satisfactorily the order of magnitude of the simulation results. The model, Eq. (1) predicts dislocation formation immediately after the start of indentation, $d = 0$. This is delayed in the simulation since dislocations need a finite stress for nucleation, which is not taken into account in the model. But then the simulation data catch up; for indentation to a depth of $d = R = 21.4$ Å, the model predicts $L_{\text{disl}} = 335$ Å, which is in good quantitative agreement with the simulation results, Table 1(a).

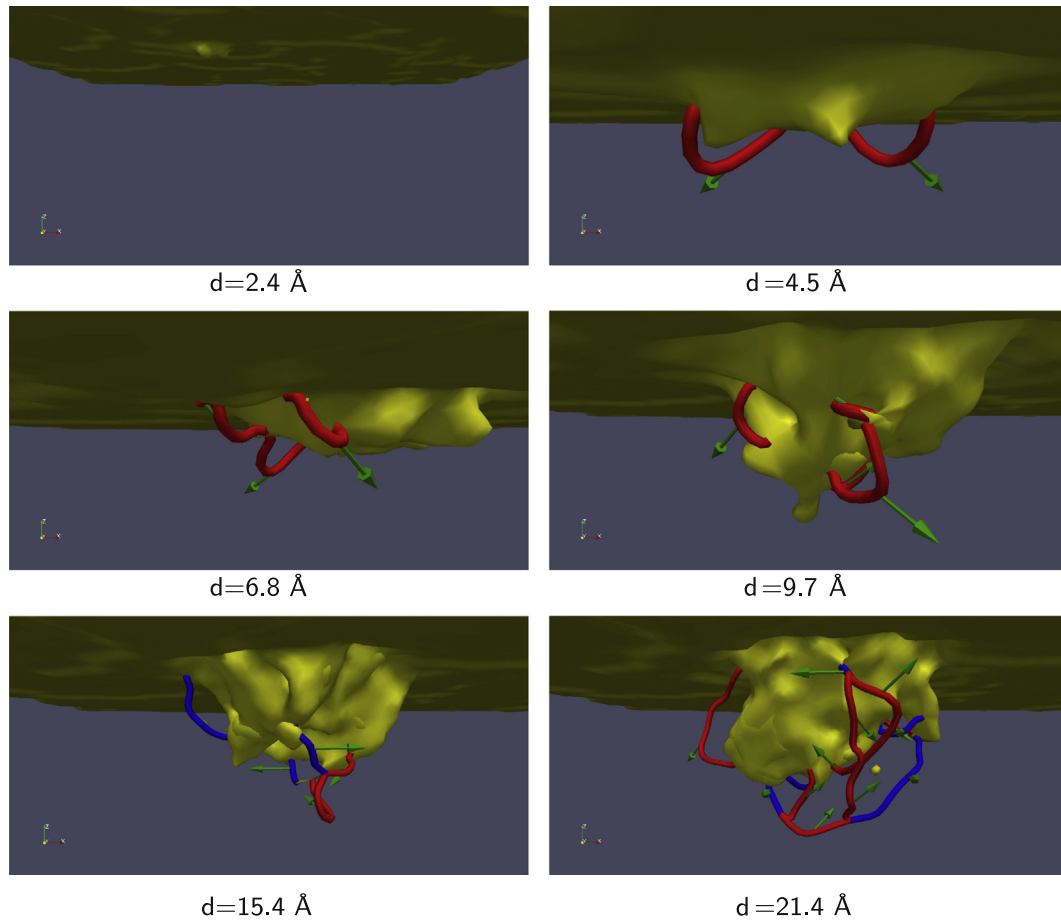


Fig. 3. Snapshots showing defect formation at various stages of the indentation process. Yellow: deformed surface including unidentified defects. Dislocation lines with Burgers vector $\mathbf{b} = \frac{1}{2}\langle 111 \rangle$ are shown in red, those with $\mathbf{b} = \langle 100 \rangle$ in blue. Green arrows indicate direction of \mathbf{b} . Dislocations are detected using the DXA algorithm [39]. Visualization has been prepared using Paraview [45]. (For interpretation of the references to colour in this figure legend, the reader is referred to the web version of this article.)

Table 1

Evolution of the dislocation network during (a) indentation and (b) scratching. d : indentation depth, ℓ : scratch length, R_{plast} : radius of plastic zone during indent, h : maximum dislocation depth, L_{disl} : total dislocation length, N_{111} : number of dislocations with Burgers vector $\mathbf{b} = \frac{1}{2}\langle 111 \rangle$, N_{100} : number of dislocations with Burgers vector $\mathbf{b} = \langle 100 \rangle$, ρ : dislocation density.

d (Å)	R_{plast} (Å)	L_{disl} (Å)	N_{111}	N_{100}	ρ (10^{17} m^{-2})
(a)					
4.5	16	57.5	2	0	7.9
6.8	25	64.2	3	0	2.2
9.7	25	63.1	4	0	2.3
15.4	49	148.0	2	4	0.6
21.4	52	369.2	9	5	1.3
ℓ (Å)	h (Å)	L_{disl} (Å)	N_{111}	N_{100}	ρ (10^{17} m^{-2})
(b)					
14.8	52	524.0	9	5	2.2
24.2	48	657.1	16	4	2.0
24.8	49	766.2	21	6	2.4
26.9	49	789.9	21	7	2.3
48.3	55	652.5	18	5	2.1
49.1	55	674.9	20	6	1.6

Our data also allow us to determine the dislocation density ρ in the plastic zone. We determine the radius of the plastic zone R_{plast} by the largest distance of a dislocation from the indent point. The data are included in Table 1(a). In the final stage, $d = 21.4$ Å, dislocations have been generated up to a radius of $R_{\text{plast}} = 52$ Å, i.e., up

to around $2.4R$. Previous studies found similar relations which may be summarized as

$$R_{\text{plast}} = f a_c. \quad (3)$$

The factor f is a constant and depends on the hardness of the material. Durst et al. [52] find that f is in the range of 0–3.5, such that our value of $f = 2.4$ is well in this range.

We approximate the volume of the plastic zone as a hemisphere with radius R_{plast} , but subtract the immersed part of the volume of the indenter [53]; this is, however, only a 10% correction. The resulting dislocation densities are displayed in Table 1 and show that the densities reach values of the order of $(1-2) \times 10^{17} \text{ m}^{-2}$.

From the above predictions for L_{disl} , Eq. (1), and the plastic-zone radius R_{plast} , Eq. (3), we obtain

$$\rho = \frac{L_{\text{disl}}}{\frac{2\pi}{3} R_{\text{plast}}^3} = \frac{1}{b R f^3}. \quad (4)$$

Note that this prediction is independent of indentation depth d , since the contact radius cancels out. For $f = 2.4$, Eq. (4) predicts $\rho = 1.2 \times 10^{17} \text{ m}^{-2}$ in good agreement with our simulation results.

Fig. 2(b) displays the evolution of the contact pressure with indentation depth. Here the contact pressure is defined as the ratio of the indentation force F_z and the projected contact area A_c ,

$$p_c(d) = \frac{F_z(d)}{A_c(d)}. \quad (5)$$

The contact area is determined from the x and y coordinates of the Fe atoms that are in contact with (that is, within the interatomic potential cut-off radius of 4.2 Å of) the indenter. A_c is calculated from an elliptical approximation to the set of these contact atoms, see Ref. [17]. The average of the contact pressure is denoted as the (normal) hardness H_z . Fig. 2(b) shows that the contact pressure reaches a constant value beyond indentation depths of ~ 10 Å; this value defines the hardness of the material. We thus find that the hardness of the Fe (100) surface is around 19.7 GPa (average over $d = 12.5$ – 21.4 Å).

It is known that due to the indentation size effect [34] mentioned in Section 1 hardness decreases monotonically with increasing depth and only reaches a steady value after about 100 nm. This behavior is attributed to the fact that with increasing indentation the contribution to hardness from pre-existing defects in the sample becomes more dominant than the tip-induced generation of plasticity [30]; note that in our simulations, the crystal is defect-free before indent, in contrast to experiments. We therefore expect that when continuing our indentation simulation to larger depths – in a larger simulation volume – a smaller hardness value would be obtained.

Lu et al. [4] determine the hardness of Fe experimentally for depths between 10 and 300 nm; they find that the hardness decreases from 4.5 to 2.5 GPa with increasing depth. When extrapolating their results to 2.86 nm – their simulation depth – they obtain 24.2 GPa. They also perform simulations using a hemispherical iron indenter; using the Shastry–Farkas potential [54] they obtain for the Fe (100) surface a hardness of 17.4 GPa, in reasonable agreement with our value.

Smith et al. [30] obtain experimentally hardnesses of 4.1 GPa and 2.2 GPa for {100} and {110} faces, respectively, for depths of < 100 nm. Towards smaller depths, hardness increases and assumes values of 6–7 GPa at depths of around 10–20 nm. Their simulated hardness is in the range of 31.4–32.5 GPa, for the Finnis–Sinclair [55] potential. We conclude that experimental hardness data are not available for Fe at indentation depths < 10 nm; extrapolations of measured data to smaller depths are, however, in agreement with the high hardnesses obtained by simulation.

Fig. 4(a) gives an additional view on the atomistic configuration of the defect structure at the last state of the indentation process. It is the same state as the last snapshot of Fig. 3, i.e., at the maximum indentation depth ($d = 21.4$ Å). A vacancy has been created under the indented surface as the result of dislocation reactions. In addition we see that a twin has been created. The twin plane is a $\langle 112 \rangle$ plane, as it is commonly found for bcc metals [47]. We note that twinning has been reported in experiments of nanoindentation into nano-crystalline Ta (grain sizes of 10–30 nm) [56]. Deformation twinning is untypical in fcc metals. These authors report that previous molecular-dynamics studies could not identify twinning in nanoindentation simulations even for bcc materials.

3.2. Scratching

After indentation the indenter tip scratches at a constant depth ($d = 21.4$ Å) in $[010]$ direction with velocity 10 m/s. During this

process we monitor the normal force, F_z , and the scratching force, F_x . Fig. 5(a) shows the data as a function of the scratching length.

The normal force decreases from its initial high value – determined by the substrate hardness – of 0.4 μN to about half this value at the end of the scratching. Most of this decrease already occurs during the first 5 Å. During this initial scratching period the lateral scratching force builds up and reaches a value of 0.15 μN ; this is close to the final value. Note that the sum of the two forces amounts to approximately the initial value, 0.4 μN . We argue that the reason for this reorientation of the indenter force lies in the organization of the dislocation network, since the origin of the forces lies in the plastic response of the specimen. While during indentation the material reacts to the vertical indentation force by building up a dislocation network, during scratching new dislocations are generated in front of the indenter in order to hinder its motion. The reorganization of the plastic zone occurs in the first 5–10 Å; afterwards both normal and lateral force acquire approximately constant values. We denote this initial phase up to $\ell = 10$ Å as the *onset regime*.

During scratching, the contact area of the indenter decreases from its initial value of 20 nm² to its final stable value of 15 nm², see Fig. 5(b). This decrease proceeds up to a scratching length of $\ell = 10$ Å, slightly later than the stabilization of the lateral and normal forces. We argue that the area decrease is caused by the fact that after starting the lateral motion, the indenter loses contact with the ‘backwards’ part of the scratch groove.

Again, we illustrate the process by a series of snapshots, Fig. 6, demonstrating the generation and reaction of dislocations. The snapshots are taken at times where normal and/or scratching force reach extreme (maximal or minimal) values.

When the scratching length reaches $\ell = 14.8$ Å both the scratching and the normal force attain minimum values. At this moment there exist 14 dislocations that have been generated under the scratched surface: 9 with Burgers vector $\mathbf{b} = \frac{1}{2}\langle 111 \rangle$ and 5 with Burgers vector $\mathbf{b} = \langle 100 \rangle$. At $\ell = 24.2$ Å both the scratching and the normal force reach a maximum. At this time the number of dislocations increases to 20; 16 with Burgers vector $\mathbf{b} = \frac{1}{2}\langle 111 \rangle$ and 4 with Burgers vector $\mathbf{b} = \langle 100 \rangle$. Similarly at the other times displayed, where the forces reach maximum or minimum values, new dislocations have been generated. The numbers are assembled in Table 1(b). Note the continuous interaction of $\mathbf{b} = \frac{1}{2}\langle 111 \rangle$ dislocations leading to the extension of the dislocation $\mathbf{b} = \langle 100 \rangle$ along the scratching direction.

This analysis of dislocation generation demonstrates that maxima and minima in the forces correspond to the rearrangement of the dislocation network: generation and/or reactions of dislocations. From Fig. 5(a) it is notable that such force maxima or minima typically exist in both the lateral and normal force simultaneously. This feature is due to the fact that the newly formed dislocations in the three-dimensional network influence both forces simultaneously.

Also, despite the relatively short length of our scratch simulation of $L = 50$ Å, we can observe a characteristic re-organization of the dislocation network. Initially, dislocations are of course centered below and around the indentation region; with increasing

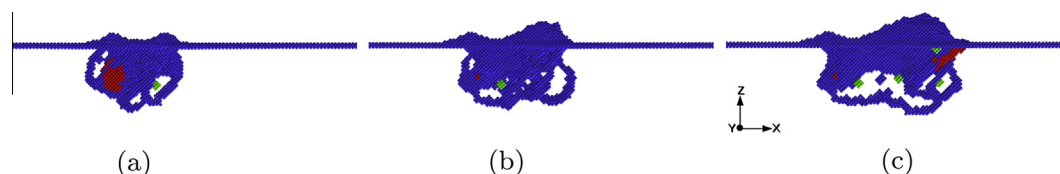


Fig. 4. Atomistic view of the crystal defect structure (a) after full indentation, $d = 21.4$ Å, cf. last subfigure of Fig. 3, (b) after scratching length $\ell = 24.8$ Å, and (c) towards the end of scratching, $\ell = 49.1$ Å, see Fig. 6. Red: twin boundary. Green: atoms surrounding vacancy. Blue: other defect atoms, including surface and dislocation cores. Defects are detected using the CAT tool [41–43]. Visualization has been prepared using OVITO [46]. (For interpretation of the references to colour in this figure legend, the reader is referred to the web version of this article.)

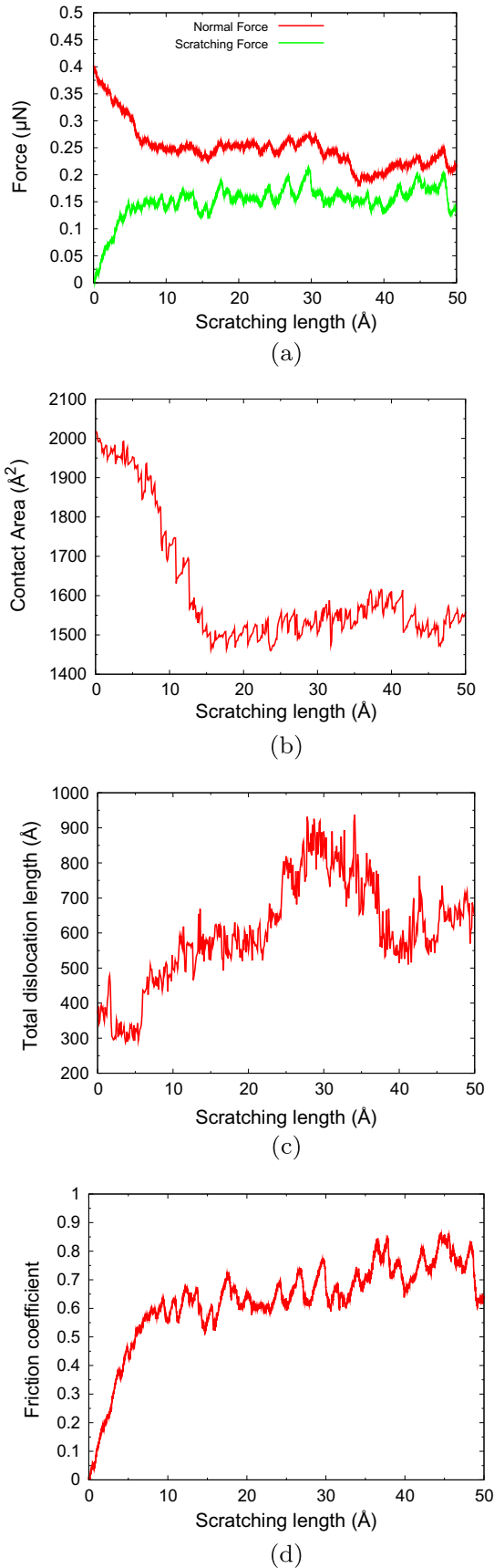


Fig. 5. (a) Normal force and scratching force, (b) contact area, (c) total dislocation length, and (d) friction coefficient as function of the scratching length during the scratching process at depth $d = 21.4$ Å.

scratch length, dislocations are newly generated at the scratch front, such that the entire scratch groove is enclosed by dislocations. Upon further scratching this high dislocation density relaxes in the middle of the groove; while dislocations are constantly newly formed at the scratch front, in the middle dislocations react until finally only a single long dislocation with Burgers vector $\mathbf{b} = \langle 100 \rangle$ remains; it connects the front and the back part of the groove. This demonstrates that the dislocation density is non-uniform along the groove, reaching high values at the start and end, and lower values along its middle part.

The dislocation reactions occurring below the middle part of the groove leave point defects (vacancies) behind. These are clearly seen in the final snapshots of Fig. 6 as isolated small yellow surfaces below the scratch groove, and also in Fig. 4(c).

This picture of dislocation network re-organization is quantified by the evolution of the total length of the dislocations, L_{disl} , as displayed in Fig. 5(c). During the *onset* period of the first 5–10 Å, the length of the dislocations does not change; thereafter it increases steadily until it reaches a maximum at around $\ell = 30$ Å scratch length. At this point the re-organization of the dislocation network starts which is signaled by a decrease of the total dislocation length. Afterwards, for $\ell = 40$ –50 Å the dislocation length remains approximately constant, fluctuating between around 500 and 700 Å. We expect, however, new dislocations to be generated and thus L_{disl} to increase again if the scratch simulation were continued beyond $L = 50$ Å.

In order to estimate the average dislocation density, we use a cuboid volume, whose dimensions are determined by the spatial extension of the dislocations. The resulting data are assembled in Table 1(b). We see that the maximum dislocation depth stays roughly constant at values of 48–55 Å, while the dislocation density attains values of around $2 \times 10^{17} \text{ m}^{-2}$. The dislocation network re-organization is also reflected in these data by the decrease of ρ after its maximum around $\ell = 30$ Å.

Besides dislocations, twins are formed also in the scratch process, as evidenced in Fig. 4. Note that the twin formed during indentation strongly decreased in size after the indenter moved away and allowed the material to relax. During scratch, initially no further twin is formed, Fig. 4(b), but eventually, at $\ell = 50$ Å scratch length a twin has formed at the scratch front which is as large as that formed after indentation.

Fig. 7 illustrates the scratch groove formed at the end of the scratch process. The groove itself has a regular form; however, the bottom shows atomic steps and is thus not uniform in depth. Note that the maximum groove depth (-24.2 Å) is deeper than the scratch depth of $d = 21.4$ Å; this is due to the repulsive indenter-substrate potential with its cut off at 4.2 Å. The form of the pile-up of the excavated atoms above the form is highly non-uniform. At the rear side we see the remnants of the indentation-induced pile-up. During the scratch *onset* not much debris is deposited on the surface; with increasing scratch, however, the pile-up increasingly grows, and reaches its maximum at the front. The pile-up is strongly asymmetrical, emphasizing debris deposition not in the $[100]$ direction in front of the scratch tip, but rather at 45° to the scratch direction. This feature is strongly reminiscent of the experimental AFM image of the nanoindentation pit formed in the Ta (100) surface [27], where the anisotropy of the debris on the surface could be traced back to the activation of the $\{110\}\langle 111 \rangle$ slip system, which brings material at 45° to the scratch direction to the surface.

Fig. 8 gives a graphical presentation of the slip generating the pile-up, which has been inspired by the corresponding work of Ref. [27] on indentation in W. For the $\{110\}\langle 111 \rangle$ slip system, the intersections of the slip directions and the slip plane with the surface coincide and lie at an angle of 45° to the advancing tip direction. For the $\{112\}\langle 111 \rangle$ slip system, the slip planes intersect

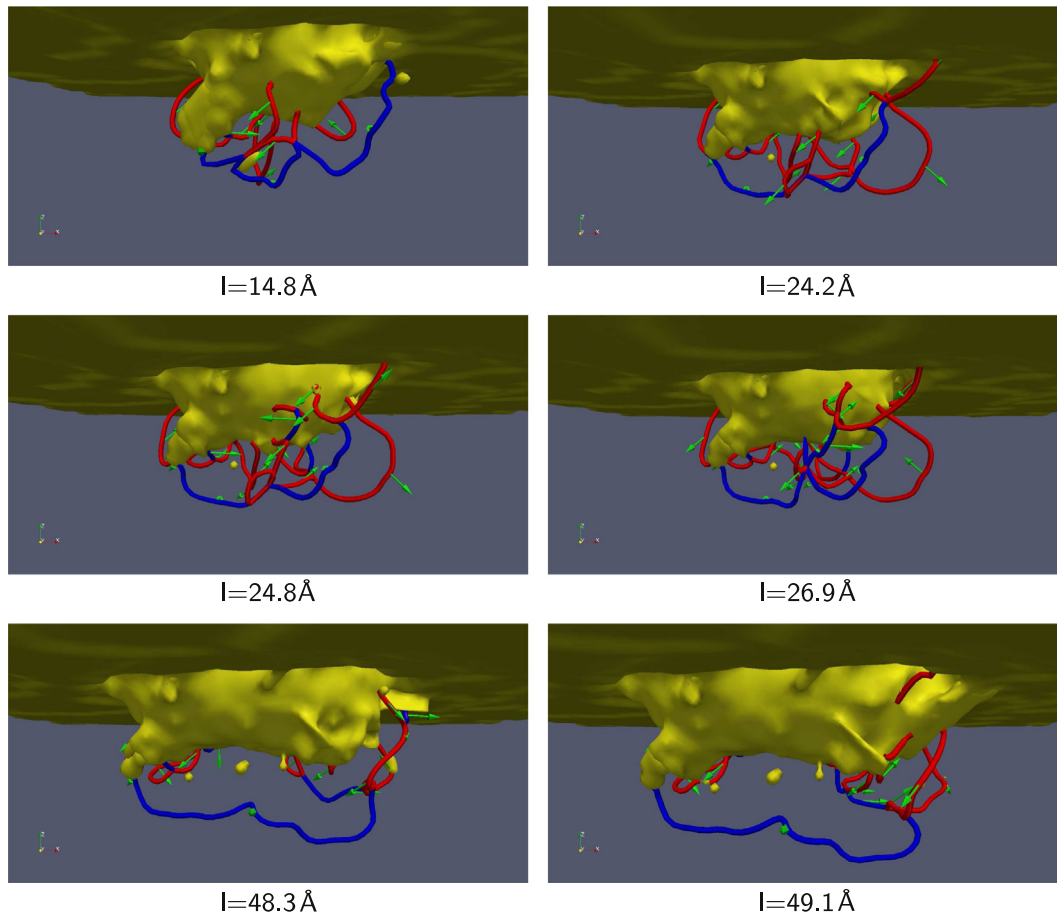


Fig. 6. Snapshots showing defect evolution at various stages of the scratching process. Color code as given in Fig. 3. Note the continuous interaction of $\mathbf{b} = \frac{1}{2}\langle 111 \rangle$ dislocations leading to the extension of the $\mathbf{b} = \langle 100 \rangle$ dislocation along the scratching direction. The isolated yellow surfaces represent vacancies left over from dislocation reactions. (For interpretation of the references to color in this figure legend, the reader is referred to the web version of this article.)

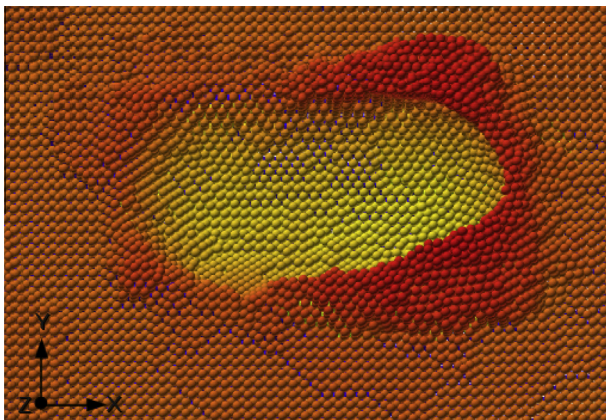


Fig. 7. Top view of the substrate after scratch along the $+x$ direction. Color codes height above surface. The deepest point in the trough is -24.2 Å, the highest in the pile-up is $+23.7$ Å above the initial surface. (For interpretation of the references to color in this figure legend, the reader is referred to the web version of this article.)

the surface both at larger and smaller angle to the advancing tip (see the dashed arrows in Fig. 8), while the intersection of the slip direction with the surface plane is of course unchanged. In result, also this slip system contributes efficiently to pile-up generation.

After scratch we retract the indenter vertically out of the groove (velocity 10 m/s). After this retraction process, the bottom of the groove and also the height of the pile-up are slightly changed: groove depth -22.3 Å, pile-up height $+25.0$ Å. This is a simple

consequence of the elastic relaxation of the material after indenter retraction.

The number of atoms missing from the groove, i.e., the empty lattice sites below the initial surface, amounts to 3778 atoms.

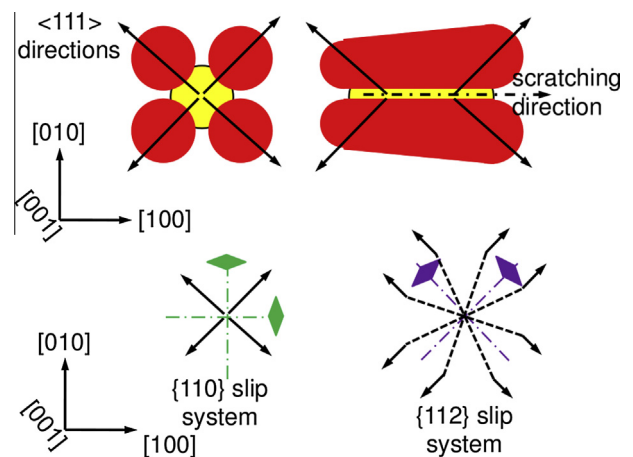


Fig. 8. Schematics showing the orientation of the intersections of the slip directions (full black arrows) and of the slip planes (dashed arrows) with the (001) surface plane to visualize the pile-up formation. Both the $\{110\}\langle 111 \rangle$ and $\{112\}\langle 111 \rangle$ slip systems contribute. During scratching the pile-ups move along the crystal. Yellow: position of indenter during indent and scratch. Red: Pile-up. Colored rhomboids show symmetry axis in surface for orientation. (For interpretation of the references to color in this figure legend, the reader is referred to the web version of this article.)

The number of atoms in the debris deposited on the surface is only 3752. The difference of 26 atoms denotes the surplus of defect atoms which have been pushed during indentation or scratching into the surrounding material.

The (instantaneous) friction coefficient is defined as the ratio of the scratching force and the normal force on the indenter,

$$\mu = \frac{F_x}{F_z}. \quad (6)$$

Fig. 5(d) shows the evolution of the friction coefficient with the scratching length. In the first 10 Å, the friction coefficient increases strongly with scratching length; during this *onset* time the scratching force builds up. After $\ell = 10$ Å, μ assumes a roughly constant value with an average of $\mu = 0.68$. Apart from the strong fluctuations visible, it shows a slowly increasing trend. As evidenced by Fig. 5, this is mainly due to the slightly decreasing normal force; the scratching force stays roughly constant.

3.3. Dependence on scratch depth

We perform scratching simulations for several scratch depths: 5.4, 10.4, and 15.4 Å.

The evolution of the friction coefficients with the scratching length is displayed in Fig. 9. Apart from the shallowest scratch, they follow the evolution of the 21.4 Å case in Fig. 5(b). After an onset period of $\ell \cong 10$ Å, the friction assumes constant values. However, here no trend of an increase (or decrease) of μ with ℓ can be read off.

The shallowest scratch, $d = 5.4$ Å, is different since here no onset region can be seen. Rather the friction coefficient slowly increases to its maximum value. An inspection of the evolution of the lateral and normal force shows for both forces a rather flat evolution with scratch length. This behavior is caused by the very shallow, near-surface scratch, in which the elastic response of the substrate still contributes significantly.

Note that immediately after indentation, $\ell = 0$, the friction coefficient is not exactly 0. This is due to the fact that the dislocation network established after indentation is non-symmetrical and exerts a small – positive or negative – force on the indenter in lateral direction.

The average values of the forces and of the friction coefficient are assembled in Table 2. In addition, we include two hardness values which are often introduced in tribological research [57,58] to characterize materials response during scratch:

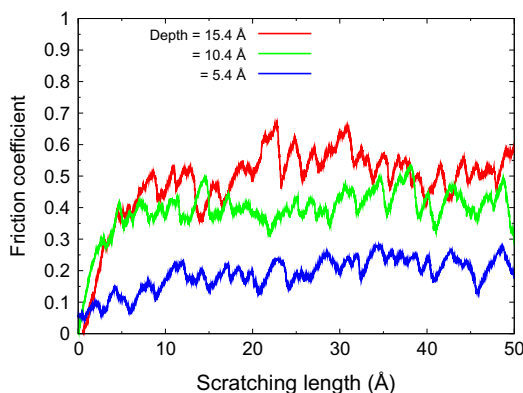


Fig. 9. Friction coefficient as function of the scratching length during scratching at various scratch depths.

Table 2

Dependence of scratching characteristics on scratch depth d . $\langle F_z \rangle$: normal force, $\langle F_x \rangle$: scratching force, $\langle \mu \rangle$: friction coefficient, H_z : normal hardness, H_x : scratching hardness. Simulation results averaged over the last 40 Å scratching length, excluding the onset region.

d (nm)	$\langle F_z \rangle$ (μN)	$\langle F_x \rangle$ (μN)	$\langle \mu \rangle$	H_z (GPa)	H_x (GPa)
0.54	0.190	0.039	0.208	29.96	37.67
1.04	0.211	0.087	0.411	19.94	31.80
1.54	0.227	0.118	0.522	17.13	25.30
2.14	0.236	0.160	0.682	16.41	22.25

- (i) The normal hardness, which is determined from the normal force and the contact area A_c projected in normal direction upon the surface plane, as in Eq. (5). In order to simplify the procedure we use a simple geometric model to estimate A_c as the area of a circle with contact radius a_c , Eq. (2):

$$A_c = \pi a_c^2 = \pi [R^2 - (R - d)^2]. \quad (7)$$

This underestimates the actual microscopic contact area, as it is based on the geometrical indenter cross section only. We can estimate the error by comparing the value obtained for full indentation, $d = R = 21.4$ Å, with the simulation result displayed in Fig. 5(b). Eq. (7) gives 1438 Å^2 ; while this value is too small during indent, it is a fair approximation under scratch.

- (ii) The lateral hardness is analogously defined as

$$H_x(d) = \frac{\langle F_x \rangle}{A_t}. \quad (8)$$

We estimate the lateral contact area A_t again in a geometrical picture as the cross section of the immersed part of the indenter onto the lateral y - z plane. It is given by a circular segment, whose area is easily calculated as

$$A_t = \frac{1}{2} R^2 (\alpha - \sin \alpha), \quad (9)$$

where the opening angle α of the circular segment is calculated from

$$\sin \frac{\alpha}{2} = \frac{a_c}{R}. \quad (10)$$

We note that in the literature, either of these hardness values is denoted as the scratching hardness. We calculated both values in order to avoid confusion. Our simulation results averaged over the scratch length – but excluding the onset regime – are collected in Table 2. We note:

- The normal force weakly increases with scratch depth d .
- The scratching force strongly increases with scratch depth d .
- The friction coefficient shows a strong increase with d ; this is due to the strong dependence of the scratching force on d .
- Both normal and lateral hardness strongly decrease with scratching depth. This is the sign of a pronounced size effect of scratching.

The behavior of the forces can be explained by the fact that both the normal and the lateral indenter cross-sectional areas increase with depth. However, as the hardness results demonstrate, the forces do not increase in proportion to the respective areas, but more strongly. We attribute this to the influence of the dislocation network generated, which leads to the well-known size effect in hardness found in indentation [34,59,60]. It is due to the ratio of the contact area to the volume of the plastically deformed zone; since the volume increases more rapidly than the area with

increasing indentation (or scratch) depth, the substrate appears softer.

Mulliah et al. [7] previously performed a nanoscratching simulation in the Fe (100) surface with a pyramid-shaped diamond indenter at 300 K. They used the Finnis–Sinclair interaction potential for Fe [55] and a pyramidal diamond tip rounded at the end with a curvature radius of 20 Å. Their calculated friction coefficient is 0.19 for the indentation depth of 5 Å, and 0.45 for the indentation depth of 15 Å, in good agreement with the present results, Table 2.

Experiments on nanoindentation of bcc materials, including Fe, were performed by Voyiadjis et al. [25]. They observe that at small indentation depths, < 10 nm, the hardness rises from a level of around 2 GPa, and reaches values of > 6 GPa at depths of 2 nm. While this value is still smaller than ours, the trend of increasing hardness for shallow indentation is compatible with our results.

4. Conclusions

Using classical molecular-dynamics simulation and the Mendelev potential we study nanoindentation and scratching in an Fe (100) surface. In the indentation stage, we find that – beyond the elastic stage and after dislocation nucleation – the total length of the dislocations increases in good agreement with a simple model based on the dislocations necessary to remove the material from the indentation zone (geometrically necessary dislocations). Both $\mathbf{b} = \frac{1}{2}\langle 111 \rangle$ and $\mathbf{b} = \langle 100 \rangle$ dislocations contribute. The dislocation density stays approximately constant.

During scratching, we observe a distinct re-organization of the dislocation network. While initially the plastic zone created by indentation simply grows – linearly with scratch length – along the scratch path, after some length dislocation reactions lead to a strong decrease of the dislocation density in the middle of the scratch. Plastic activity then is concentrated only on the scratch front. Only few dislocations remain in the middle of the scratch. Vacancies in this zone are created by dislocation reactions that occurred here. The continuous interaction of $\mathbf{b} = \frac{1}{2}\langle 111 \rangle$ dislocations leads to the extension of $\mathbf{b} = \langle 100 \rangle$ dislocations along the scratching direction.

Both in the indentation and in the scratching stage we find point defects – vacancies generated by dislocation reactions – and deformation twinning.

During the scratch, maxima (and minima) in the lateral and normal force give evidence of dislocation generation and reaction processes. Interestingly, these maxima always occur simultaneously in the lateral and the normal force, since dislocations exert their forces in both directions.

Our results for the scratch stage show a strong depth effect: with increasing scratch depth, the material appears to soften, as evidenced by the measured average hardness in lateral and normal direction. This depth dependence is more pronounced for the lateral force than for the normal force. In consequence, the friction coefficient strongly increases with increasing depth.

Acknowledgment

We acknowledge support by the Deutsche Forschungsgemeinschaft via the Sonderforschungsbereich 926.

References

- [1] A.C. Fischer-Cripps, *Nanoindentation*, 2nd ed., Springer, New York, 2004.
- [2] A. Gouldstone, N. Chollacoop, M. Dao, J. Li, A.M. Minor, Y.-L. Shen, *Acta Mater.* 55 (2007) 4015.
- [3] I. Szlufarska, *Mater. Today* 9 (2006) 42.

- [4] C. Lu, Y. Gao, G. Michal, G. Deng, N.N. Huynh, H. Zhu, X. Liu, A.K. Tieu, *J. Nanosci. Nanotechnol.* 9 (2009) 7307.
- [5] G. Ziegenhain, H.M. Urbassek, *Philos. Mag.* 89 (2009) 2225.
- [6] G. Ziegenhain, A. Hartmaier, H.M. Urbassek, *J. Mech. Phys. Sol.* 57 (2009) 1514.
- [7] D. Mulliah, S.D. Kenny, E. McGee, R. Smith, A. Richter, B. Wolf, *Nanotechnology* 17 (2006) 1807.
- [8] R.W. Carpick, M. Salmeron, *Chem. Rev.* 97 (1997) 1163.
- [9] K.J. Van Vliet, J. Li, T. Zhu, S. Yip, S. Suresh, *Phys. Rev. B* 67 (2003) 104105.
- [10] X.-L. Ma, W. Yang, *Nanotechnology* 14 (2003) 1208.
- [11] T. Zhu, J. Li, K.J. Van Vliet, S. Ogata, S. Yip, S. Suresh, *J. Mech. Phys. Sol.* 52 (2004) 691.
- [12] H. Liang, C.H. Woo, H. Huang, A.H.W. Ngan, T.X. Yu, *Comput. Model. Eng. Sci.* 6 (2004) 105.
- [13] A. Asenjo, M. Jaafar, E. Carrasco, J.M. Rojo, *Phys. Rev. B* 73 (2006) 075431.
- [14] T. Tsuru, Y. Shibutani, *Phys. Rev. B* 75 (2007) 035415.
- [15] S.-P. Ju, C.-T. Wang, C.-H. Chien, J.-C. Huang, S.-R. Jian, *Mol. Simul.* 33 (2007) 905.
- [16] E. Carrasco, O. Rodríguez de la Fuente, J.M. Rojo, *Philos. Mag.* 88 (2008) 281.
- [17] G. Ziegenhain, H.M. Urbassek, A. Hartmaier, *J. Appl. Phys.* 107 (2010) 061807.
- [18] W. Paul, D. Oliver, Y. Miyahara, P.H. Grütter, *Phys. Rev. Lett.* 110 (2013) 135506.
- [19] R. Komanduri, N. Chandrasekaran, L.M. Raff, *Wear* 240 (2000) 113.
- [20] D. Mulliah, D. Christopher, S.D. Kenny, R. Smith, *Nucl. Instrum. Meth. B* 202 (2003) 294.
- [21] D. Mulliah, S.D. Kenny, R. Smith, C.F. Sanz-Navarro, *Nanotechnology* 15 (2004) 243.
- [22] S. Jun, Y. Lee, S.Y. Kim, S. Im, *Nanotechnology* 15 (2004) 1169.
- [23] T.-H. Fang, C.-H. Liu, S.-T. Shen, S.D. Prior, L.-W. Ji, J.-H. Wu, *Appl. Phys. A* 90 (2008) 753.
- [24] J.J. Zhang, T. Sun, A. Hartmaier, Y.D. Yan, *Comput. Mater. Sci.* 59 (2012) 14.
- [25] G.Z. Voyiadjis, A.H. Almasri, T. Park, *Mech. Res. Commun.* 37 (2010) 307.
- [26] J.H.A. Hagelaar, E. Bitzek, C.F.J. Flipse, P. Gumbsch, *Phys. Rev. B* 73 (2006) 045425.
- [27] M.M. Biener, J. Biener, A.M. Hodge, A.V. Hamza, *Phys. Rev. B* 76 (2007) 165422.
- [28] J. Alcalá, R. Dalmáu, O. Franke, M. Biener, J. Biener, A. Hodge, *Phys. Rev. Lett.* 109 (2012) 075502.
- [29] D. Christopher, R. Smith, A. Richter, *Nanotechnology* 12 (2001) 372.
- [30] R. Smith, D. Christopher, S.D. Kenny, A. Richter, B. Wolf, *Phys. Rev. B* 67 (2003) 245405.
- [31] C. Lu, Y. Gao, G. Michal, N.N. Huynh, H.T. Zhu, A.K. Tieu, *Proc. IME J. J. Eng. Tribol.* 223 (2009) 977.
- [32] N.N. Kumar, R. Tewari, P.V. Durgaprasad, B.K. Dutta, G.K. Dey, *Comput. Mater. Sci.* 77 (2013) 260.
- [33] C. Lu, Y. Gao, G. Michal, H. Zhu, N. Huynh, and A. Tieu, in *Advanced Tribology* edited by J. Luo, Y. Meng, T. Shao, and Q. Zhao, Springer, Berlin, 2010, pp. 562–563.
- [34] K. Durst, B. Backes, O. Franke, M. Göken, *Acta Mater.* 54 (2006) 2547.
- [35] R. Komanduri, N. Chandrasekaran, L.M. Raff, *Phys. Rev. B* 61 (2000) 14007.
- [36] M.I. Mendeleev, S. Han, D.J. Srolovitz, G.J. Ackland, D.Y. Sun, M. Asta, *Philos. Mag.* 83 (2003) 3977.
- [37] S. Banerjee, S. Naha, I.K. Puri, *Appl. Phys. Lett.* 92 (2008) 233121.
- [38] S. Plimpton, *J. Comput. Phys.* 117 (1995) 1. <<http://lammps.sandia.gov/>>.
- [39] A. Stukowski, K. Albe, *Model. Simul. Mater. Sci. Eng.* 18 (2010) 085001.
- [40] D. Faken, H. Jonsson, *Comput. Mater. Sci.* 2 (1994) 279.
- [41] A. Stukowski, V.V. Bulatov, A. Arsenlis, *Model. Simul. Mater. Sci. Eng.* 20 (2012) 085007.
- [42] A. Stukowski, *Model. Simul. Mater. Sci. Eng.* 20 (2012) 045021.
- [43] A. Stukowski, A. Arsenlis, *Model. Simul. Mater. Sci. Eng.* 20 (2012) 035012.
- [44] J. Li, *Model. Simul. Mater. Sci. Eng.* 11 (2003) 173. <http://li.mit.edu/Archive/Graphics/Al/>.
- [45] A. Henderson, *Paraview guide*, A Parallel Visualization Application, Kitware Inc, 2007. <<http://www.paraview.org>>.
- [46] A. Stukowski, *Model. Simul. Mater. Sci. Eng.* 18 (2010) 015012. <http://www.ovito.org/>.
- [47] A. Kelly, K.M. Knowles, *Crystallography and Crystal Defects*, second ed., John Wiley, Chichester, UK, 2012.
- [48] D.A. Terentyev, Y.N. Osetsky, D.J. Bacon, *Acta Mater.* 58 (2010) 2477.
- [49] M.S. De Guzman, G. Neubauer, P. Flinn, W.D. Nix, *Mater. Res. Soc. Symp. Proc.* 308 (1993) 613.
- [50] W.D. Nix, H. Gao, *J. Mech. Phys. Sol.* 46 (1998) 411.
- [51] J.G. Swadener, E.P. George, G.M. Pharr, *J. Mech. Phys. Sol.* 50 (2002) 681.
- [52] K. Durst, B. Backes, M. Göken, *Scr. Mater.* 52 (2005) 1093.
- [53] J. Hua, A. Hartmaier, *Model. Simul. Mater. Sci. Eng.* 18 (2010) 045007.
- [54] V. Shastry, D. Farkas, *Model. Simul. Mater. Sci. Eng.* 4 (1996) 473.
- [55] M.W. Finnis, J.E. Sinclair, *Philos. Mag.* A 50 (45) (1984); M.W. Finnis, J.E. Sinclair, *Erratum* 53 (1986) 161.
- [56] Y.M. Wang, A.M. Hodge, J. Biener, A.V. Hamza, D.E. Barnes, K. Liu, T.G. Nieh, *Appl. Phys. Lett.* 86 (2005) 101915.
- [57] V. Blank, M. Popov, G. Pivovarov, N. Lvova, K. Gogolinsky, V. Reshetov, *Diamond Relat. Mater.* 7 (1998) 427.
- [58] F. Wredenberg, P.-L. Larsson, *Wear* 266 (2009) 76.
- [59] G.M. Pharr, G. Herbert, Y. Gao, *Annu. Rev. Mater. Res.* 40 (2010) 271.
- [60] M.A. Lodes, A. Hartmaier, M. Göken, K. Durst, *Acta Mater.* 59 (2011) 4264.